Fabrication and characterization of iron and fluorine co-doped BST thin films for microwave applications

F. Stemme · M. Bruns · H. Geßwein · M. Schroeder · M. Sazegar ·
M. D. Drahus · R.-A. Eichel · F. Paul · C. Azucena · J. R. Binder

Abstract The effects of fluorine co-doping by means of a post-thermal annealing process of iron-doped BST thin films in a fluorine-containing atmosphere have been investigated. XPS and ToF-SIMS sputter depth profiling verified a homogeneous fluorine distribution in the thin films. By employing EPR, it was shown that singly charged $(Fe'_{Ti}–V^{..}_O)^.$ defect complexes, as well as 'isolated' Fe'_{Ti} centres with a distribution of $F^._O$ sites in remote coordination spheres exist in the fluorinated films. Tunability enhancement due to fluorine co-doping as well as a Q-factor enhancement due to iron doping is demonstrated.

Introduction

The tunable dielectric barium strontium titanate ($Ba_{1-x}Sr_x TiO_3$, BST) is one of the most promising materials for microwave applications in the GHz range. It may be used in phase shifters or tunable filters [1–5]. The incorporation of acceptor and donor dopants in the materials structure is an effective way to tailor the materials properties. Paul et al. [6] and Zhou et al. [7] presented a transition metal-fluorine co-doping in screen-printed BST thick films as a suitable way to achieve low material losses and an acceptable tunability in the microwave range up to 30–40 GHz. Regarding the influence of the microstructure on the dielectric properties Friederich et al. [8], Zhou et al. [9] and Paul et al. [10] have shown that the mean grain diameter strongly influences the tunability of the thick films. Thus, the influence of grain size or crystal quality superimposes the influence originating from the dopants. However, acceptor–donor co-doping using fluorine as donor dopant has not yet been demonstrated for thin films. We modified a radio frequency (RF) co-sputter process to introduce iron as an acceptor dopant into BST thin films [11] and demonstrated the influence of the acceptor dopant

F. Stemme · H. Geßwein · M. Schroeder · J. R. Binder (✉)
Institute for Applied Materials (IAM-WPT), Karlsruhe Institute of Technology, Hermann-von-Helmholtz-Platz 1, 76344 Eggenstein-Leopoldshafen, Germany
e-mail: joachim.binder@kit.edu

F. Stemme · F. Paul
Department of Microsystems Engineering, IMTEK, University of Freiburg, Georges-Köhler-Allee 102, 79110 Freiburg, Germany

M. Bruns
Institute for Applied Materials (IAM-ESS), Karlsruhe Institute of Technology, Hermann-von-Helmholtz-Platz 1, 76344 Eggenstein-Leopoldshafen, Germany

M. Bruns
Karlsruhe Nano Micro Facility (KNMF), Karlsruhe Institute of Technology, Hermann-von-Helmholtz-Platz 1, 76344 Eggenstein-Leopoldshafen, Germany

M. Sazegar
Institute for Microwave Engineering and Photonics, Technische Universität Darmstadt, Merckstraße 25, 64283 Darmstadt, Germany

M. D. Drahus
Department of Physical Chemistry, University of Freiburg, Albertstraße 21, 79104 Freiburg, Germany

R.-A. Eichel
Research Centre Juelich, Institute of Energy and Climate Research (IEK 9), 52435 Jülich, Germany

C. Azucena
Institute of Functional Interfaces (IFG), Karlsruhe Institute of Technology, Hermann-von-Helmholtz-Platz 1, 76344 Eggenstein-Leopoldshafen, Germany

Fig. 1 Schematic illustration of the influence of fluorination in iron doped BST thin films, exemplarily shown for one perovskite unit cell
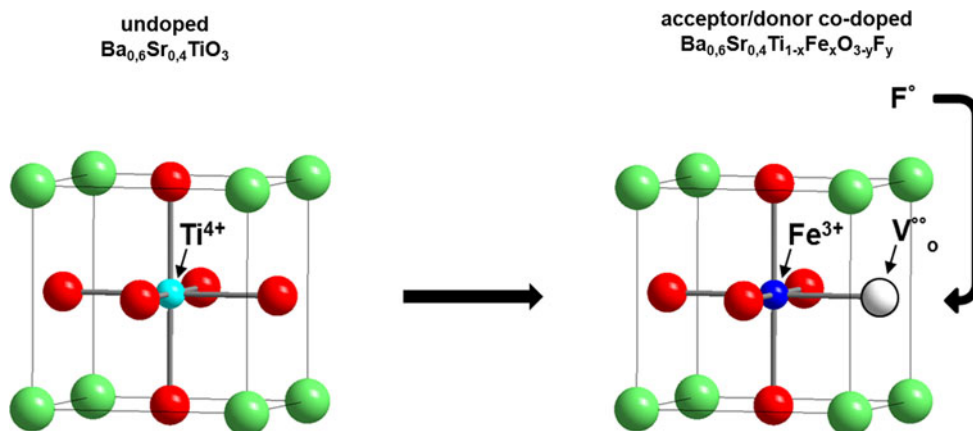
without the superimposing influence of the microstructure [12]. The enhanced Q-factor at 1 GHz in the co-sputtered thin films, which is associated with a reduced material loss factor tanδ due to the iron doping, is also coupled with a reduced tunability and permittivity resulting from the defect structure in the material. By annealing BST thin films in different atmospheres, many researchers tried to improve the materials' properties by modifying the defect structure, e.g. reducing the amount of oxygen vacancies [13–17]. Analogous to this strategy, we annealed iron acceptor-doped BST thin films in fluorine containing atmosphere, to introduce fluorine as a donor dopant on the oxygen site of the perovskite structure, which simultaneously reduces the concentration of oxygen vacancies and prevents a significant change of the thin film microstructure. The principle of the fluorination process of the BST thin films is schematically depicted in Fig. 1, where the unit cell of the BST structure is shown.

The B-site dopants Fe^{2+} and Fe^{3+} have a lower valence than the host ion Ti^{4+} (Fe''_{Ti}, Fe'_{Ti}), and therefore oxygen vacancies are formed for reasons of charge compensation, creating either neutral or singly positive charged defect complexes like $(Fe''_{Ti}–V_O^{··})^x$ or $(Fe'_{Ti}–V_O^{··})^·$. These defect complexes have a positive influence on the material loss factor tanδ and their existence could be experimentally verified in BST [11, 12] and $Sr(Ti_{1-x}Fe_x)O_3$ powder [18–21].

The chemical binding states of the iron dopant were obtained from X-ray photoelectron spectroscopy (XPS) and time-of-flight secondary ion mass spectroscopy (ToF-SIMS). Sputter depth profiling provides the depth distribution of the dopant. Incorporation of the dopant in the crystal structure and complementary to XPS, the Fe^{3+} content and the defect structure of the material was monitored by electron paramagnetic resonance spectroscopy (EPR). Grazing incident X-ray diffraction (GIXRD) and Raman spectroscopy were used to validate the crystal structure. Detailed investigations of the morphology of the BST thin films were performed by scanning electron microscopy (SEM) and atomic force microscopy (AFM). For microwave characterization, a Metal–Insulator–Metal (MIM) capacitor setup was used.

Experimental

Film preparation

The BST thin film deposition, with a nominal BST target composition of $Ba_{0.6}Sr_{0.4}TiO_3$, was realized in a RF sputtering setup using a 3″ ION'X planar magnetron source (TFC, Grafenberg, Germany) mounted on a standard double-cross recipient equipped with a pre-sputter shutter and a sample positioner allowing various working distances (150–200 mm) between magnetron and substrate. The planar magnetron was perpendicular to the sample holder. The gas inlet was equipped with an MKS mass-flow control system (MKS Instruments Deutschland GmbH, München) providing a constant operating pressure of 1×10^{-2} mbar of 80 vol. % Ar and 20 vol. % O_2 for reactive sputtering. To achieve a base pressure of $<5 \times 10^{-6}$ mbar for sufficient purity, a turbomolecular pumping unit was used. The RF sputtering power was 85 W (PFG 300 power supply, Hüttinger, Freiburg, Germany) leading to deposition rates of about 14–20 nm/h with a target substrate distance of about 150 mm. During sputter deposition, no internal heating was used.

The first post-deposition annealing process was carried out in a furnace with a silicon dioxide tube and ambient atmosphere for approximately 1 h at 800 °C with a heating and cooling rate of 5 °C/min.

The BST powder required for EPR measurements was produced by sputter-deposition of thin films onto polyimide foil. The material was removed from the foil by solvent-free scraping and was finally annealed in a differential scanning calorimeter (DSC) with a heating rate of

5 °C/min under synthetic air using the same temperature and duration time as for the thin films.

For microwave characterization, a 20 nm thick Cr adhesive layer and 1 μm thick gold top electrode were RF sputtered onto the BST films and structured by etching process.

Co-sputter target and substrates

To design the co-sputter target, iron foil stripes (Goodfellow, Bad Nauheim, Germany) of 1.5×25 mm^2 were radially fixed with the target clamp ring at equal distances onto a circular 3″ $Ba_{0.6}Sr_{0.4}TiO_3$ ceramic base target (Kurt J. Lesker Ldt., UK) (for details see ref [11]). Various amounts of such foils were used to tune the iron stoichiometry within the films via the resulting target area ratios of the dopant and the BST base target [11, 12, 22, 23]. For the dielectric characterization in a metal–insulator–metal (MIM) configuration, Pt(150 nm)/ TiO$_2$(20 nm)/SiO$_2$(300 nm)/Si(0.5 mm) substrates with sizes of about 17×17 mm^2 were used (Inostek Inc., Korea). Before the BST film deposition the substrates were thoroughly rinsed in isopropanol and dried with clean air.

Fluorination process

To introduce fluorine as a co-dopant on the oxygen site of the perovskite structure, the iron-doped BST thin films were subjected to a second annealing process in a fluorine containing atmosphere, which provides diffusion-controlled fluorination of the BST thin films. The setup is schematically shown in Fig. 2. This second post-deposition annealing step was performed in a tube furnace with an Al$_2$O$_3$ tube under dried, purified air for approximately 4 h at 700 °C above fluorine-containing powder bed in a covered platinum crucible. The powder bed was a highly
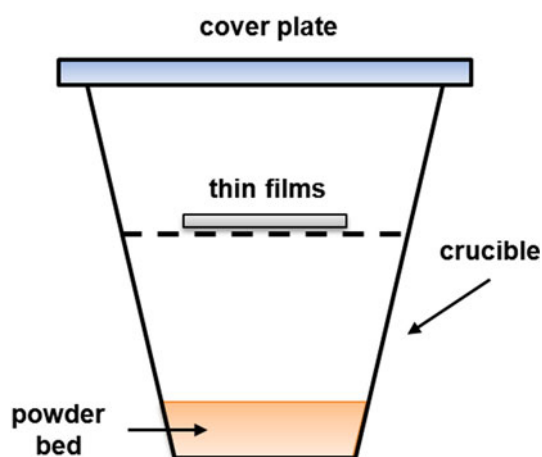

Fig. 2 Schematic illustration of the experimental setup for the fluorination process

fluorine doped, spray dried BST powder synthesized by a modified sol–gel process [6, 7].

Film characterization

XPS measurements were performed using a K-Alpha XPS spectrometer (ThermoFisher Scientific). Data acquisition and processing using the Thermo Avantage software is described elsewhere [24]. All BST thin films were analysed using a microfocused, monochromated Al Kα X-ray source (200 μm spot size). The K-Alpha charge compensation system was employed during analysis using electrons of 8 eV energy and low-energy argon ions to prevent any localized charge build-up. The spectra were fitted with one or more Voigt profiles (binding energy uncertainty: ±0.2 eV). The analyser transmission function, Scofield sensitivity factors [25] and effective attenuation lengths (EALs) for photoelectrons were applied for quantification. EALs were calculated using the standard TPP-2M formalism [26]. All spectra were referenced to the C 1s peak of hydrocarbon at 285.0 eV binding energy controlled by means of the well-known photoelectron peaks of metallic Cu, Ag and Au, respectively.

XPS sputter depth profiling was performed using a 1 keV Ar$^+$ ion beam at a raster size of 2×4 mm^2 and a 30° angle of incidence. Film thicknesses of 200 nm were estimated by XPS sputter depth profiles referenced to sputter yields achieved from well-defined electrochemically fabricated 100 nm Ta$_2$O$_5$/Ta substrates and scanning electron microscopy (SEM) fracture pattern.

ToF-SIMS was performed on a TOF.SIMS^5 instrument (ION-TOF GmbH, Münster, Germany), equipped with a Bi cluster liquid metal primary ion source and a non-linear time of flight analyser. The Bi source was operated in the 'bunched' mode providing 0.7 ns Bi1$^+$ ion pulses at 25 keV energy and a lateral resolution of approx. 4 μm. Negative polarity spectra were calibrated on the C$^-$, C$_2^-$, C$_3^-$ and Li$^-$ peaks. Positive polarity spectra were calibrated on the C$^+$, CH$^+$, CH$_2^+$ and CH$_3^+$ peaks. Sputter depth profiles were performed using a 1 keV Cs$^+$ ion beam and a raster size of 400×400 μm^2.

The crystal structure of doped BST thin films was validated by grazing incident X-ray diffraction using a Bruker D8 diffractometer with CuKα radiation in parallel beam setup. A Goebel mirror was inserted in the primary beam and parallel plate collimators were placed in the diffracted beam. A fixed incident angle of α = 2° was used during the 2θ scans (Bruker AXS GmbH, Karlsruhe, Germany).

Raman measurements were performed with the LabRam HR Raman confocal microscope (Horiba Scientific) operating in a 180° backscattering geometry. Each BST thin film sample was measured by focusing the laser beam onto small areas about 1 μm^2 using the laser wavelength of

442 nm (He-Cd laser) and a laser power of 25 mW. Several spots on BST thin films were illuminated for four seconds and spectra were recorded 30 times to optimize phonon intensities.

X-Band (9.8 GHz) EPR measurements to study the incorporation of the iron dopant and the defect structure of the sputtered BST were performed using a Bruker EMX spectrometer (Bruker BioSpin GmbH, Rheinstetten, Germany) at ambient temperature. For the exact calibration of the magnetic field, an NMR gaussmeter (ER 035M, Bruker) and a standard field marker polycrystalline Diphenylpicrylhydrazyl (DPPH) with $g = 2.0036$ were used.

Morphology of the thin films was investigated using a Carl Zeiss Supra 55VP scanning electron microscope (Carl Zeiss AG, Oberkochen, Germany) and an Asylum MFP-3D-Bio atomic force microscope (Asylum Research, Santa Barbara, USA). The AFM was operated at 25 °C in an isolated chamber in intermittent contact mode. A single NSC-35 AFM-cantilever (MikroMasch, Germany) with a resonance frequency 315 kHz and spring constant 14 N/m was used for all the images.

For microwave characterization, MIM structures were fabricated on the thin films and were measured using an on-wafer characterisation setup. An RF impedance/material Analyser (Agilent E4991A) was used to measure the capacitance and Q-factor of the devices. The MIM structures were contacted with a ground-signal-ground on-wafer probe. The internal bias source of the E4991A was used to apply the tuning voltage.

Results and discussion

Elemental composition and dopant distribution

XPS core level spectra of the fabricated iron-doped (sample a) and iron/fluorine co-doped (sample b) BST thin films are shown in Fig. 3. The surface elemental composition of the iron doped and iron/fluorine co-doped thin films are almost identical. Binding energies of the element-specific photoelectrons of the BST components are in good accordance with binding energies reported in literature [11, 27, 28]. In particular, Ba $4d_{5/2} = 88.3$ eV is attributed to the Ba^{2+} component, Sr $3d_{5/2} = 133.1$ eV, is found for Sr^{2+} and the corresponding O^{2-} component appears at O $1s = 529.7$ eV in iron and iron/fluorine-doped BST thin films, respectively. The binding energy of the Ti^{4+} component is 458.4 eV in both cases and for the Ti^{3+} component at 457.4 eV. The additional peaks in the Ba $4d$ and O $1s$ spectra indicated in Fig. 3 are related to surface components and contaminations (see ref [11]).

The Fe $2p$ binding energies of the iron components in the iron-doped BST thin films are found at 709.9 eV for Fe^{2+}, 711.9 eV for Fe^{3+} and a Fe^{2+} loss feature at 714.1 eV [29]. In the case of iron/fluorine co-doped BST thin films, the binding energy for Fe^{2+} is 710.9 eV, for Fe^{3+} 712.9 eV and for the Fe^{2+} loss feature 714.8 eV, which is actually 1 eV higher than in the iron-doped films and indicates the successful fluoride incorporation. Films that had undergone the same annealing regime, but without fluorine exposure, do not show such high energy shifts. As expected, a strong signal at 685.2 eV developed in the F $1s$. All findings are in good agreement with literature results for, e.g. pure FeF_2 [30].

The distribution of the dopants in the BST thin films was monitored by XPS and complementary ToF-SIMS sputter depth profiling. The XPS sputter depth profile of an iron-doped BST thin film annealed in a fluorine-containing atmosphere in Fig. 4 proves a homogenous distribution of all the BST-related elements. It is clearly to be seen that bottom platinum electrode is not affected by the thermal annealing in a fluorine-containing atmosphere either and no interdiffusion between the BST thin film and the platinum electrode occurred. Even the iron concentration is very homogeneous throughout the film, cf. inset of Fig. 4, whereas the fluorine concentration slightly increases towards the bottom electrode. The achieved dopant concentration is about 2.4 ± 0.2 at. % Fe and 1.8 ± 0.2 at. % F. It has to be noted that it is impossible to monitor the oxidation state of the dopant throughout the film due to sputter induced reduction during the depth profiling [31]. The corresponding ToF-SIMS sputter depth profiles shown in Fig. 5 support the XPS findings. Moreover, the fragments TiO_2F^- and $FeOF^-$ prove the desired coordination of fluoride to Ti and Fe.

Defect structure

The formation of associated defects, exemplarily shown for Fe'_{Ti}, is described by Eq. 1 [32]

$$Fe'_{Ti} + V_O^{\cdot\cdot} \leftrightarrow \left(Fe'_{Ti} - V_O^{\cdot\cdot}\right)^{\cdot} \tag{1}$$

which defines a temperature and oxygen partial pressure-dependent equilibrium constant

$$K_{ass} = \frac{\left[\left(Fe'_{Ti} - V_O^{\cdot\cdot}\right)^{\cdot}\right]}{\left[Fe'_{Ti}\right]\left[V_O^{\cdot\cdot}\right]}. \tag{2}$$

The electroneutrality condition for iron-doped BST can be written as

$$\left[Fe'_{Ti}\right] \approx 2\left[V_O^{\cdot\cdot}\right] + \left[h^{\cdot}\right] \tag{3}$$

so that one $V_O^{\cdot\cdot}$ compensates two iron centres. In the case of fluorine doping, Eq. 3 should be modified as

$$\left[Fe'_{Ti}\right] \approx 2\left[V_O^{\cdot\cdot}\right] + \left[h^{\cdot}\right] + \left[F_O^{\cdot}\right] \tag{4}$$

with electron holes $h^{\cdot}$ and fluoride $F_O^{\cdot}$ as donor dopant.
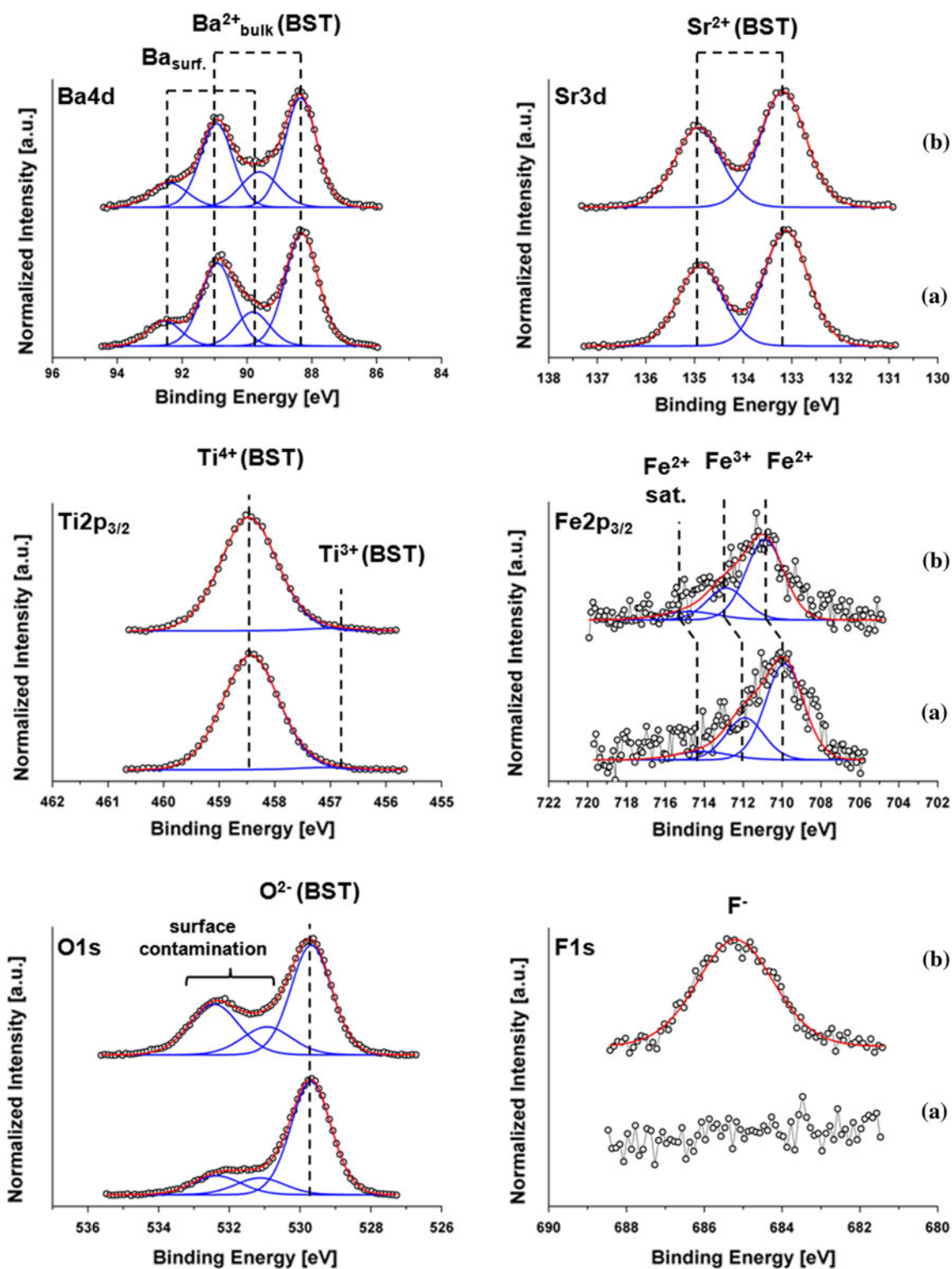
Fig. 3 XPS spectra of **a** non-fluorinated and **b** fluorinated iron-doped BST thin films. Spectra are normalized to maximum intensity

The defect structure of the sputtered BST powder was probed by EPR spectroscopy [33]. Figure 6 compares the spectra of an iron-doped BST reference powder annealed at 800 °C for 1 h (sample a) with the spectra of a powder which was additionally post-annealed at 700 °C for 4 h in a fluorine-containing atmosphere (sample b). Two resonances at 340 and 150 mT can be clearly observed. These are attributed to the Fe^{3+} incorporated at B-sites of the
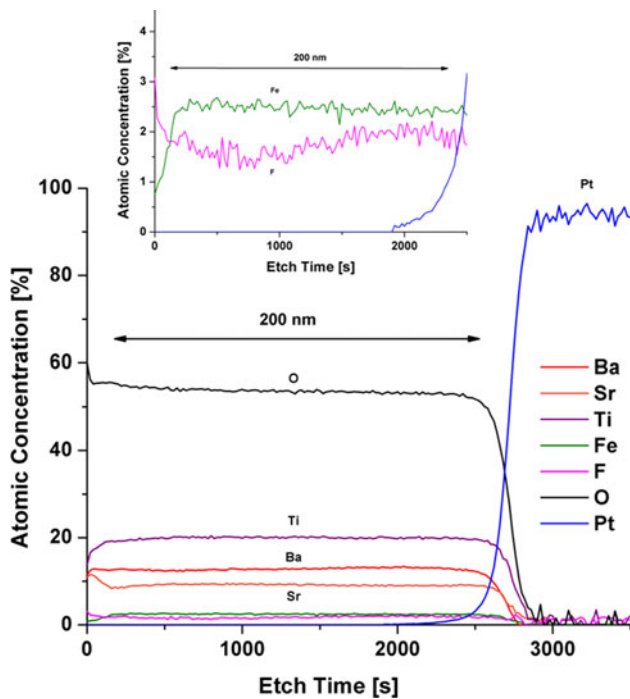
Fig. 4 XPS sputter depth profile of a fluorinated, iron-doped BST thin film. Film thickness is approximately 200 nm. Magnification of the iron and fluorine signal is depicted in the inset
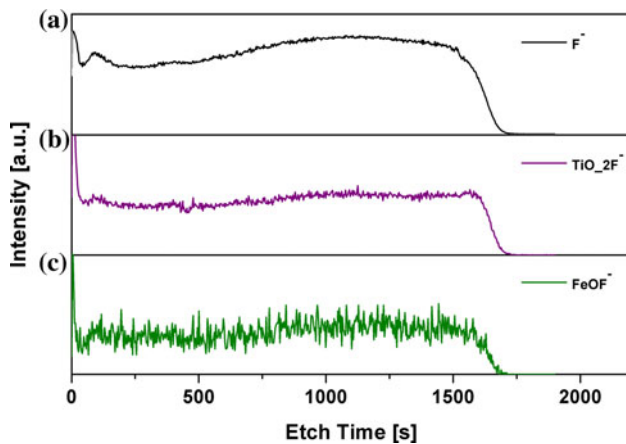

Fig. 5 ToF-SIMS sputter depth profile of a fluorinated, iron-doped BST thin film. Displayed is the depth distribution of the F^-, TiO_2F^- and $FeOF^-$ masses

perovskite structure, Fe'_{Ti}, without oxygen vacancies located in the first coordination sphere [11, 12, 18, 19, 34] and the $(Fe'_{Ti}-V_O^{\cdot\cdot})^{\cdot}$ defect dipole complex [35, 36], respectively. While the line shapes of the these two spectra are similar, there is an approximately 33 % increase in the 'Peak to Peak' line width of the fluorinated sample in comparison to the non-fluorinated sample indicating the existence of magnetically active ions in the vicinity of the
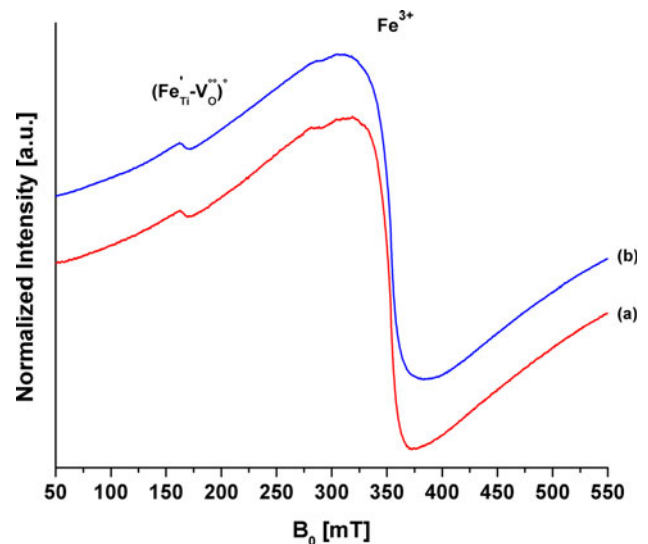

Fig. 6 EPR spectra of iron-doped sputtered BST powder after annealing for **a** 1 h @ 800 °C in ambient air and **b** 1 h @ 800 °C in ambient air and for 4 h @ 700 °C in a fluorine-containing atmosphere

paramagnetic Fe^{3+} centres. Because of the strong magnetic moment of fluoride, this observation is tentatively assigned to $F_O^{\cdot}$ centres. As this hyperfine interaction rather leads to a line broadening than to a distinct hyperfine splitting in the EPR spectra, a considerable distribution of $F_O^{\cdot}$ sites along different crystallographic orientations and several coordination spheres has to be taken into account. This describes a picture of a fluoride distribution in remote unit cells surrounding the Fe^{3+} centres.

No decrease in intensity of the resonance at low fields due to the fluorination could be observed, which implies a stable defect complex in the first coordination sphere. But, with respect to the EPR and XPS data, the strong influence of the fluoride on the iron dopant can be demonstrated. These results indicate that an incorporation of the fluoride donor dopant only took place either in not-associated oxygen vacancies in remote unit cells, in oxygen vacancies which are associated with Fe'_{Ti}, over several unit cells which are not detectable by EPR, or in oxygen vacancies which are associated with the Fe''_{Ti} and also not detectable by X-Band EPR.

Crystal structure and morphology

The crystal structure of the BST thin films after different thermal treatments was investigated by grazing incident X-ray diffraction and diffraction patterns are compared in Fig. 7. All thin films have a cubic perovskite structure with $Pm-3m$ space group symmetry. The additional diffraction peaks which are not BST related are due to the multilayer substrate or sample holder. The strong peaks at approximately 40° 2theta and 47° 2theta can be assigned to the
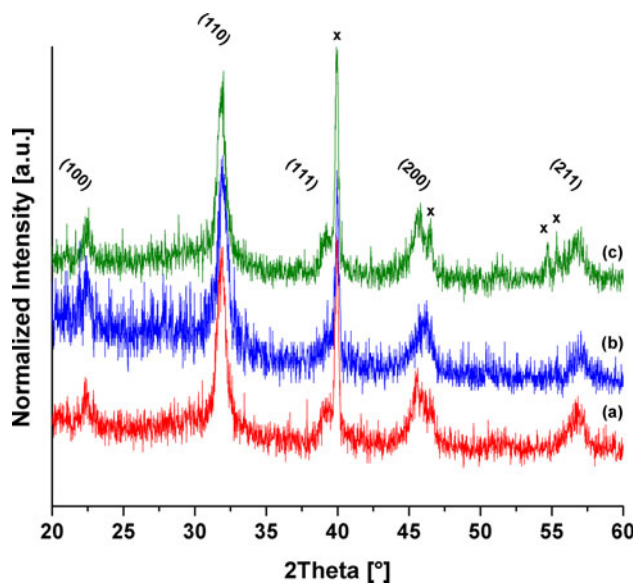
Fig. 7 XRD patterns of iron-doped BST thin films annealed in different atmospheres. **a** 1 h @ 800 °C in ambient air, **b** 1 h @ 800 °C in ambient air and additional 4 h @ 700 °C in ambient air, and **c** 1 h @ 800 °C in ambient air and 4 h @ 700 °C in a fluorine-containing atmosphere. Substrate related reflexes are marked by '*x*'

Fig. 8 Raman spectra of BST thin films annealed **a** for 1 h @ 800 °C in ambient air, **b** for 1 h @ 800 °C in ambient air and additional 4 h @ 700 °C in ambient air, and **c** for 1 h @ 800 °C in ambient air and 4 h @ 700 °C in a fluorine-containing atmosphere

platinum bottom electrode of the metal–insulator–metal setup used for microwave characterization. No crystalline impurities due to the post-annealing process can be detected.

Raman spectra of the samples treated with different atmospheres are shown in Fig. 8. The spectra show characteristic broad vibrational bands in the phononic region below 900 cm^{-1}. Two high frequency modes at ~530 and 750 cm^{-1} and two low frequency modes at ~170 and ~270 cm^{-1} can be detected and assigned to vibrational modes of mixed ($A_1 + E$) symmetry and A_1 symmetry [37, 38]. The low frequency phonons reflect the statistical cation ordering. A broadening of the low frequency peaks corresponds to B-site doping as a result of increased structural disorder and small deviations in the overall crystal bonding. The Raman spectra of the Fe/F co-doped samples in comparison to Fe-doped BST samples show a significant decreased intensity of the broad band at ~750 cm^{-1}. This mode is usually considered to be unique for the tetragonal phase. Changes of the intensity and shape of the ~750 cm^{-1} and the ~530 cm^{-1} band are usually discussed to correspond to local cation doping effects at the TiO$_6$ octahedra [39–41]. B-site doping with iron results in a change of the relative intensities of the high frequency mode, the intensity of the ~750 cm^{-1} band increases relatively to the ~530 cm^{-1} band [12]. The decrease of the intensity of the ~750 cm^{-1} vibrational band of fluorine co-doped samples may have its origin in a local change of octahedral bonding. The substitution of small amounts of oxygen with fluoride and/or the diffusion of fluoride to
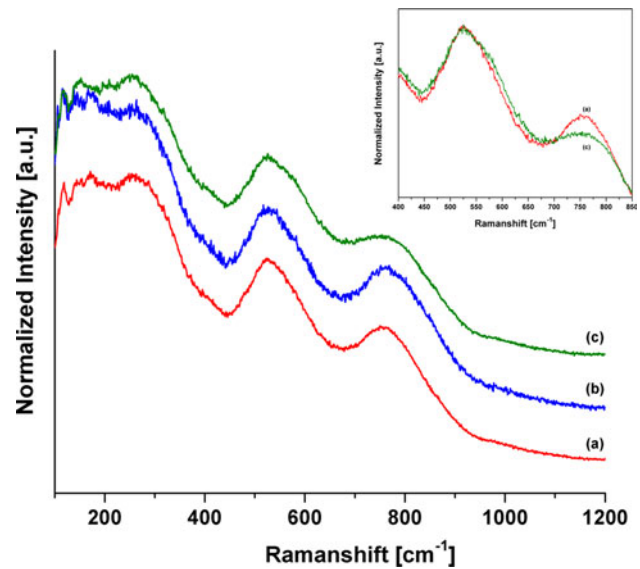
oxygen vacancies may have several consequences: 1. The presence of more electronegative fluoride will increase the overall ionicity of the octahedral bonding. As a result the Raman intensity of bands which are mainly determined by the Ti/Fe–O bonds decreases due to a lower Raman activity of vibrational modes involving less covalent bonds. 2. The local octahedral symmetry of some TiO$_6$ or FeO$_6$ is slightly distorted as a result of the non-equivalent bonds or interactions with additional fluorine/fluoride atoms/ions resulting in a slight broadening of the ~750 cm^{-1} vibrational band and a seeming decrease of intensity. 3. The presence of ionic interactions might cause a preferred orientation of the octahedra. If this preferred orientation countervails the tetragonal distortion of the unit cells in the BST film, a decrease of the intensity of the ~750 cm^{-1} band will be the consequence. But, to clarify this issue, polarized Raman experiments would be necessary [41].

Thin film morphology was investigated by scanning electron and atomic force microscopy. SEM images are depicted in Fig. 9a and the corresponding AFM images are shown in Fig. 9b. No film destruction or abnormal grain growth can be observed in the BST thin films after the post-annealing processes in different atmospheres. To quantify the surface roughness, the R_{rms} values were determined by AFM. For comparison the mean R_{rms} values of at least three measured areas of 1 mm^2 with its standard deviation is used. The R_{rms} value of the iron doped reference film, which was annealed for 1 h at 800 °C in ambient air, is about 1.9 ± 0.1 nm. After annealing the BST thin films, a second time for 4 h at 700 °C in ambient air the R_{rms} value
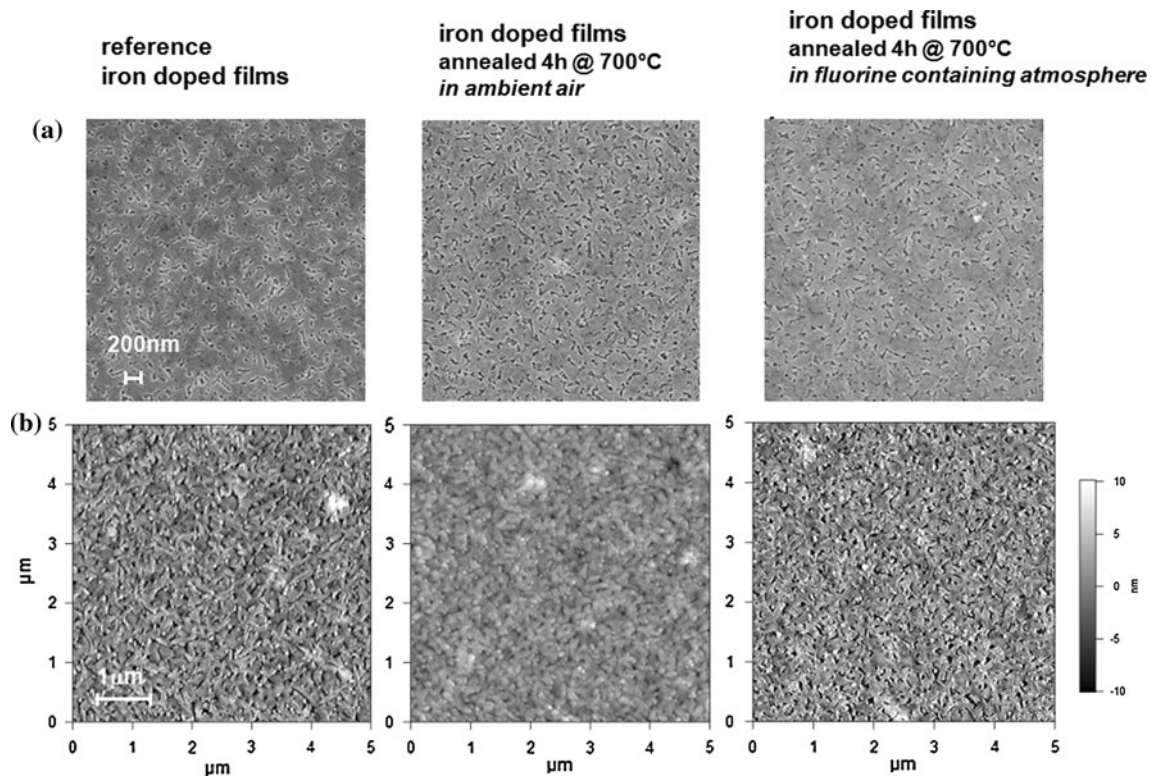
Fig. 9 REM and AFM topography images of differently processed BST thin films

slightly decreases to 1.5 ± 0.1 nm. A further slight increase of the R_{rms} value up to 2.9 ± 0.2 nm can be observed after annealing the BST thin films for 4 h at 700 °C in a fluorine-containing atmosphere. Thus, the impact of co-doping on the microwave properties can be investigated without a microstructure effect.

Dielectric characterization in the microwave range

For dielectric characterization in the microwave range (0.5 – 3 GHz), BST thin films with a constant thickness of $h_{BST} = 200$ nm were used. Using the metal–insulator–metal (MIM) capacitor, the permittivity of the material can be calculated by Eq. 5

$$\varepsilon_r = \frac{C \cdot h_{BST}}{\varepsilon_0 A_{Pad}} \quad (5)$$

with the measured capacitance C, and the MIM electrode geometry A_{Pad}.

The reduction of the materials permittivity achieved by applying an electrostatic field E, denoted as tunability, can be expressed as

$$\tau(E) = \frac{\Delta\varepsilon_r(E)}{\varepsilon(E=0)} = \frac{\varepsilon(E=0) - \varepsilon(E)}{\varepsilon(E=0)} \quad (6)$$

The used quality factor Q_{tot} is the measured loss of the whole capacitor consisting of both the losses in the metal electrodes (Q_C) and the losses in the dielectric (Q_{BST}).

$$\frac{1}{Q_{tot}} \approx \frac{1}{Q_C} + \frac{1}{Q_{BST}} \quad (7)$$

For comparison the mean value of the calculated permittivity, the tunability and the quality factor of at least three pads with its standard deviation is used.

The influence of the different processing steps on the microwave properties was studied and is compiled in Fig. 10. The untuned permittivity ($E = 0$) shows a strong variation as a function of the used dopant and annealing atmosphere, cf. Fig. 10a. Regarding the values at 1 GHz (see Table 1), it is obvious that undoped BST thin films show the highest permittivity ($\varepsilon_r = 535 \pm 12$). When iron is introduced as a B-site acceptor dopant, the permittivity decreases ($\varepsilon_r = 348 \pm 5$). This decrease can be due to different mechanisms. Introducing iron on the titanium site can lead to a distortion of the perovskite structure that causes a Curie temperature (T_C) shift and was already demonstrated for bulk ceramics [42]. But, regarding the quite flat temperature dependence for fine grained ceramics and thin films other mechanisms must take place. Here, on the other hand, a so-called internal bias field
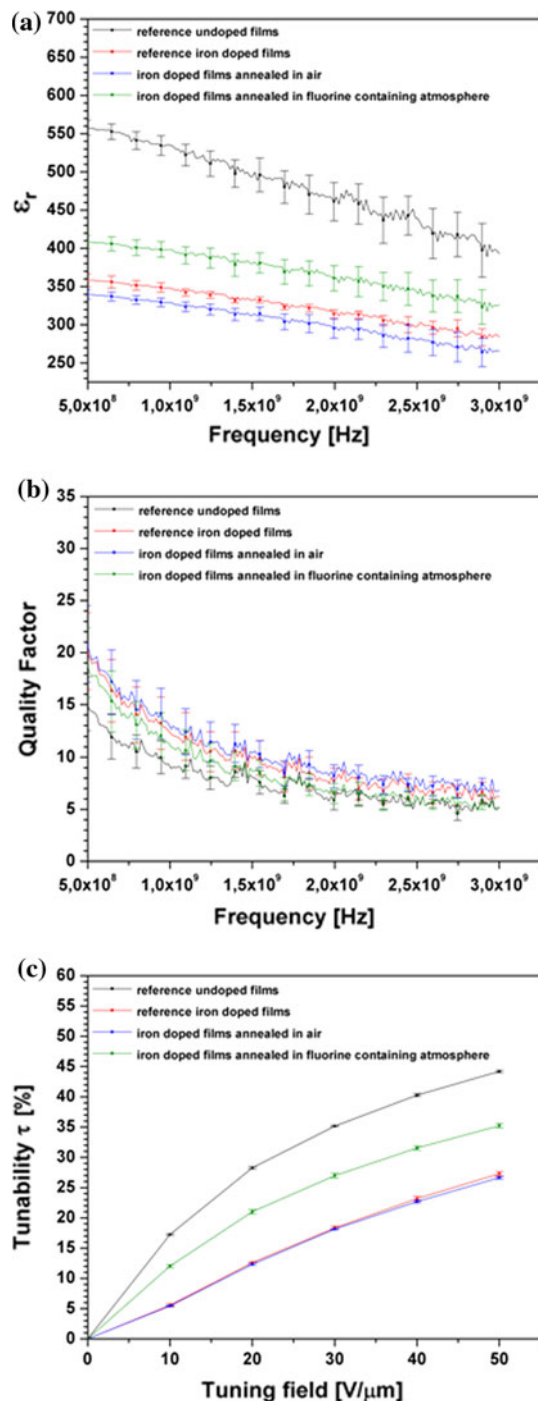
Fig. 10 a Permittivity at an effective tuning field of 0 V/μm, **b** Q-factor at an effective tuning field of 0 V/μm, and **c** tunability at 1 GHz of iron BST thin films annealed in various atmospheres. As a reference permittivity, Q-factor and tunability of an undoped BST thin film are also shown

produced by the $(Fe'_{Ti}–V^{··}_O)^·$ defect dipoles, which were detected by EPR spectroscopy, (see Fig. 6) [11, 12] and indirectly by low frequency characterization in [6] can be

formed. The impact of this internal bias field on the dielectric properties of paraelectric materials differs from that in ferroelectric materials [43–47], but it is likely that polarization mechanisms are pinned in analogy to the results given by Lohkämper et al. [43] and Warren et al. [47]. Annealing the singly iron-doped BST thin films in a fluorine-containing atmosphere leads to an increase of the untuned permittivity at 1 GHz ($\varepsilon_r = 398 \pm 11$). In contrast to this, nearly no variation of the untuned permittivity ($\varepsilon_r = 329 \pm 6$) can be detected when the BST thin films were post-annealed in ambient air. This increased permittivity when using fluoride ions as a co-dopant might be due to the diffusion of the fluoride into oxygen vacancies. The pinning of polarization mechanisms decreases and consequently the ability of polarization of the material and its permittivity increases.

However, in the EPR spectra of Fig. 6 the signal of the $(Fe'_{Ti}–V^{··}_O)^·$ defect dipole complex is also present in the fluorinated sample. This is an indication that the defect dipole complex does not change within the first coordination sphere even when fluoride ions are incorporated into the structure.

Figure 10b shows the variation of the component quality factor Q_{tot} when different annealing conditions are used. The component Q-factor Q_{tot} depends on the material quality factor and the quality factor of the metal electrodes (see Eq. 7). The decrease of Q_{tot} with increasing frequency is due to the increase of the ohmic losses in the metal electrodes [48]. The untuned Q-factor ($E = 0$ V) at 1 GHz shows the expected behaviour for undoped and iron-doped BST thin films. The shown data represent the arithmetic mean of three measurements for different pad geometries. The Q-factor Q_{tot} of the undoped BST thin film is 8.9 ± 1.4 and that of the iron doped BST thin film is 12.2 ± 2.3. This increase of the Q-factor is ascribed to the existence of the defect dipole complex as explained in our previous work [12], which affects the material loss factor in a positive way.

The tunability τ of the material annealed in different atmospheres at 1 GHz and 50 V/μm is shown in Fig. 10c. It is obvious that iron doping causes a strong decrease of the tunability from 44.2 ± 0.2 % to 27.3 ± 0.4 %, influenced by the materials defect structure. An additional annealing treatment in ambient air at 700 °C for 4 h does not change the tunability (26.6 ± 0.2 %.). A strong enhancement of the tunability can be achieved using fluorine as a co-dopant. Fluorination of the BST thin film leads to an increase of the tunability up to 35.2 ± 0.4 %. It was found that only in the presence of iron as an acceptor dopant the tunability can be increased through the fluorination process and the incorporated fluoride ions act as donor dopants.

Table 1 Annealing parameters and dielectric performance of BST thin films

Sample	Annealing parameter		Quality factor Q_{tot} ($E = 0$; 1 GHz)	ε_r ($E = 0$; 1 GHz)	τ @ 50 V/μm [%] (1 GHz)
	Duration/temperature	Atmosphere			
Reference undoped	1 h 800 °C	Ambient air	8.9 ± 1.4	535 ± 12	44.2 ± 0.2
Reference iron doped	1 h 800 °C	Ambient air	12.2 ± 2.3	348 ± 5	27.3 ± 0.4
Iron doped	1 h 800 °C/4 h 700 °C	Ambient air/ambient air	12.7 ± 2.2	329 ± 6	26.6 ± 0.2
Iron/Fluorine co-doped	1 h/800 °C/4 h 700 °C	Ambient air/fluorine containing atmosphere	11.0 ± 1.9	398 ± 11	35.2 ± 0.4

Conclusion

The influence of fluorine as a donor co-dopant on the oxygen site in iron acceptor-doped BST thin films was investigated. A nearly homogenous fluorine distribution without fluorine-containing second phases can be proved, which highlights the used post-annealing process in a fluorine-containing atmosphere as a suitable thermal process to achieve fluorine co-doping without a significant change of the microstructure. The high energy shift of the iron binding energy gives evidence of a strong influence of the fluorine co-dopant on the iron acceptor dopant on the B-site of the perovskite structure. The evolving defect structure due to the co-doping was probed with EPR spectroscopy and it was shown that the singly charged $(Fe'_{Ti}–V^{\cdot\cdot}_O)^{\cdot}$ defect complexes persist in the fluorinated films. Through the application of suitable co-dopants, it is possible to tailor the dielectric properties of BST thin films in the microwave range, i.e. using the acceptor dopant iron for the low losses and the co-dopant fluorine to enhance the tunability. In contrast to [6], the positive influence of fluorine co-doping on tunability at high frequencies was demonstrated.

References

1. Miranda FA, van Keuls FW, Romanofsky RR, Mueller CH, Alterovitz S, Subramanyam G (2002) Integr Ferroelectr 42:131
2. Cole MW, Toonen RC, Ivill M, Hirsch SG, Ngo E, Hubbard C (2011) J Appl Phys 110:124105
3. Kong LB, Li S, Zhang TS, Zhai JW, Boey FYC, Ma J (2010) Prog Mater Sci 55:840
4. Cole MW, Toonen RC, Hirsch SG, Ngo E, Romanofsky RR, van Keuls F, Hubbard C, Ivill M, Demaree D (2009) J Appl Phys 111:68
5. Tangantsev AK, Sherman VO, Astafiev KF, Venkatesh J, Setter N (2003) J Electroceram 11:5
6. Paul F, Giere A, Menesklou W, Binder JR, Scheele P, Jakoby R, Haußelt J (2008) Inter J Mater Res 10:1119
7. Zhou X, Geßwein H, Sazegar M, Giere A, Paul F, Jakoby R, Binder JR, Haußelt J (2010) J Electroceram 24:345
8. Friederich A, Zhou X, Sazegar M, Haußelt J, Jakoby R, Hoffmann MJ, Binder JR (2012) J Eur Ceram Soc 32:875
9. Zhou X, Sazegar M, Stemme F, Haußelt J, Jakoby R, Binder JR (2012) J Eur Ceram Soc http://dx.doi.org/10.1016/j.jeurceramsoc.2012.06.021
10. Paul F, Menesklou W, Link G, Zhou X, Haußelt J, Binder JR (2012) Submitted to J Appl Phys
11. Stemme F, Geßwein H, Drahus MD, Holländer B, Azucena C, Binder JR, Eichel RA, Haußelt J, Bruns M (2012) Anal Bioanal Chem 403:643
12. Stemme F, Bruns M, Geßwein H, Schroeder M, Sazegar M, Drahus MD, Eichel RA, Haußelt J, Binder JR (2012) J Mater Sci 47:6929. doi:10.1007/s10853-012-6640-7
13. Knauss LA, Pond JM, Horwitz JS, Chrisey DB, Mueller CH, Treece R (1996) Appl Phys Lett 69(1):25
14. Joo JH, Jeon YH, Seon JM, Oh KY, Roh JS, Kim JJ (1997) Jpn J Appl Phys 36:4382
15. Chen PC, Miki H, Shimamoto Y, Matsui Y, Hiratani M, Fujisaki Y (1998) Jpn J Appl Phys 37:5112
16. Kim SG, Mah SB, Jang NW, Paik DS, Park CY (1998) Mater Lett 43:254
17. Xu J, Menesklou W (2004) J Eur Ceram Soc 24:1735
18. Merkle R, Maier J (2003) Phys Chem Chem Phys 5:2297
19. Drahus MD, Jakes P, Erdem E, Eichel RA (2011) Solid State Ionics 184:47
20. Berney R, Cowan D, Morin F (1978) Solid State Commun 26:579
21. Morin F, Oliver J (1973) Phys Rev B 8:5847
22. Lutz H, Bruns M, Link F, Baumann H (1998) Thin Solid Films 332:230
23. Lutz H, Bruns M, Link F, Baumann H (1999) Surf Coat Tech 116–119:419
24. Parry KL, Shard AG, Short RD, White RG, Whittle JD, Wright A (2006) Surf Interface Anal 38:1497
25. Scofield JH (1976) J Electron Spectr Relat Phen 8:129
26. Tanuma S, Powell CJ, Penn DR (1993) Surf Interface Anal 21:165
27. Moulder JF, Stickle WF, Sobol PE, Bomben KD (1992) Handbook of x-ray photoelectron spectroscopy. Perkin-Elmer Corporation, Minesota
28. Viviani M, Buscaglia MT, Nanni P, Pardi R, Gemme G, Dacca A (1999) J Eur Ceram Soc 19:1047
29. Brundle CR, Chuang TJ, Wandelt K (1977) Surf Sci 68:459
30. Grosvenor AP, Kobe BA, Biesinger MC, McIntyre NS (2004) Surf Interface Anal 36:1564
31. Óvári L, Kiss J (2006) Appl Surf Sci 252:8624
32. Smyth DM (2000) The defect chemistry of metal oxides. Oxford University Press, New York
33. Erdem E, Jakes P, Parashar SKS, Kiraz K, Somer M, Rüdiger A, Eichel R-A (2010) J Phys: Condens Matter 22:345901

34. Warren WL, Dimos D, Tuttle BA, Smyth DM (1994) J Am Ceram Soc 77:2753
35. Jakes P, Erdem E, Eichel RA, Jin L, Damjanovic D (2011) Appl Phys Lett 98:072907
36. Siegel E, Müller KA (1979) Phys Rev B 19:109
37. Bouyanfif H, Wolfman J, El Marssi M, Yuzyuk Y, Bodeux R, Gervais M, Gervais F (2009) J Appl Phys 106:034108
38. Kuo SY, Liao WY, Hsieh WF (2001) Phys Rev B 64:224103
39. Pokorný J, Um Pasha, ben L, Thakur OP, Sinclair DC, Reanev IM (2011) J Appl Phys 109:114110
40. Zheng H, Csete de Gyorgyfalva GDC, Quimby R, Bagshaw H, Ubic R, Reanev IM, Yarwood J (2003) J Eur Ceram Soc 23:2653
41. Yuzyuk YI (2012) Phys Solid State 54:1026
42. Menesklou W, Paul F, Zhou X, Elsenheimer H, Binder JR, Ivers-Tiffée E (2011) Microsyst Technol 17:203
43. Lohkämper R, Neumann H, Arlt G (1990) J Appl Phys 68:4220
44. Robels U, Zadon Ch, Arlt G (1992) Ferroelectrics 133:163
45. Hagemann HJ (1978) J Phys C: Solid State Phys 11:3333
46. Carl K, Härdtl KH (1978) Ferroelectrics 17:473
47. Warren WL, Dimos D, Tuttle BA, Pike GE, Al-Shareef HN (1997) Integrated Ferroelectrics 16:77
48. Bao P, Jackson TJ, Wang X, Lancaster MJ (2008) J Appl Phys D 41:063001